TALLINN UNIVERSITY OF TECHNOLOGY

Faculty of Science

Chair of Oceanography

SEA ICE MONITORING FROM INTERFEROMETRIC SAR IMAGERY IN WESTERN ESTONIAN COASTAL SEA IN 2012

Bachelor's thesis

Kaari Laanemäe

Supervisor: MSc Sander Rikka

Co-supervisor: PhD Rivo Uiboupin

Marine System Institute at Tallinn University of Technology

Earth Sciences

2015

Declaration

Hereby I declare that this bachelor thesis, my original investigation and achievement, submitted for the bachelor degree at Tallinn University of Technology has not been submitted for any academic degree. All content and ideas drawn directly or indirectly from external sources are indicated as such.

Kaari Laanemäe

(Signature and date)

Supervisor: *Sander Rikka*

Work meets the requirements for bachelor's thesis.

(Signature and date)

The defence chief:

Accepted for defence of a thesis

……

(Name, signature, date)

TALLINNA TEHNIKAÜLIKOOL

Matemaatika-loodusteaduskond

Okeanograafia õppetool

MEREJÄÄ SEIRE INTERFEROMEETRILISTELT SAR PILTIDELT LÄÄNE-EESTI RANNIKUMERES 2012. AASTAL

Bakalaureusetöö

Kaari Laanemäe

Juhendaja: MSc Sander Rikka

Kaasjuhendaja: PhD Rivo Uiboupin

Meresüsteemide Instituut

Maa-teadused

2015

ABSTRACT

Current study is focused on distinguishing between different ice types using mean coherence and backscattering values of sea ice types calculated from high resolution interferometric SAR images acquired over coastal sea in the Gulf of Riga and Väinameri. Images with available incidence angles and imaging modes are compared and it is determined that for best discrimination of ice types, imaging mode has to be the same for both images used for coherence calculations and high incidence angle (over 40º) must be used.

It is determined that automated differentiation of ice types using coherence and backscattering values is possible, however using this method ice types can be falsely classified. Current study demonstrates that coherence values based on interferometric SAR data could be used to find irregularities in ice structures as ice cracks.

Key words: ice type, interferometric SAR, coherence, backscattering

LÜHIKOKKUVÕTE

Käesolev töö keskendub erinevate jäätüüpide eristamisele Riia lahe ja Väinamere rannikumeres. Metoodika põhineb jäätüüpide keskmise koherentsuse ja tagasipeegeldumise väärtuste võrdlemisel, kasutades arvutamiseks kõrgresolutsioonilisi interferomeetrilisi SAR pilte. Võrreldakse erinevaid kaldenurki ehk radariantenni ja nadiiri vahelisi nurki ja pildistamise režiime. Võrdlusest selgub, et parim tulemus jäätüüpide eristamisel saadakse, kui koherentsuse arvutamisel kasutatakse pilte, millel on sama pildistamise režiim ja suur (üle 40º) kaldenurk.

Tõestatakse, et automatiseeritud jäätüüpide eristamine, kasutades koherentsuse ja tagasipeegeldumise väärtusi, on võimalik, kuid seda meetodit kasutades on võimalik jäätüüpe valesti klassifitseerida. Käesolev töö demonstreerib, et interferomeetriliste SAR piltide koherentsuse väärtusi saab kasutada leidmaks jää pinnas ebatasasusi, näiteks jääpragusid.

Märksõnad: jää tüüp, interferomeetriline SAR, koherentsus, tagasipeegelduvus

Table of Contents

Abstract 4

Lühikokkuvõte 5

1 Introduction 8

2 Objectives 10

3 Background 11

3.1 TanDEM-X 11

3.2 Parameters calculated from interferometric SAR data 12

4 Data 14

4.1 Interferometric TDX SAR data 14

4.2 *In situ* measurements and meteorological data 15

4.3 Moderate Resolution Imaging Spectroradiometer data 15

5 Method 16

5.1 SAR backscatter and coherence 16

5.2 Relating coherence and backscattering values with ice types and water 17

6 Results 18

6.1 Identified ice types 18

6.2 Effect of incidence angle and polarization 18

6.3 Coherence and backscattering values of different ice types 21

6.4 Coherence images for area of interest 23

6.5 Ice map based on coherence and backscattering values 25

7 Discussion 27

7.1 Limitations to ice type classification 27
7.2 Interpretation of multi-source data 28
8 Conclusion 31
Acknowledgement 32
List of references 33
Appendices 37
Appendix A. Examples of fast ice (old), thin smooth ice and pancake ice 37
Appendix B. MODIS images of Gulf of Riga from 29. January to 6. February 2012 39

INTRODUCTION

The primary reasons for studying sea ice are winter navigation and environmental interests. Sea transport on the Baltic Sea is very active. According to Statistics Estonia in 2014 around 11 000 vessels navigated to and from Estonian ports, and there is no significant decrease of sea traffic during winter period (Statistika andmebaas). Accident analysis of winter navigation on the Finnish waters (Banda *et al.* 2015) reveals that the highest number of accidents has been reported when a ship is navigating independently. To avoid accidents caused by difficult ice conditions, precise information about ice structures is needed to evaluate what type of vessels could safely navigate in the said conditions.

Similarly there is an increasing interest in climate and environmental changes. The amount of sea ice cover is related to a strong feedback mechanism. Unlike water, sea ice has a high albedo. Melting of sea ice reduces albedo which causes proportionally larger increase of net solar radiation. Therefore, the amount of sea ice can be important indicator of changes in the climate. (Vihma and Haapala, 2009)

Sea ice has been monitored for more than 100 years from coastal stations and ships. The usage of aircrafts and satellites has made the sea ice monitoring operational and information can be collected from large areas simultaneously. First satellite sensors used for sea ice monitoring operated in the range of visible light and infrared frequencies. Those channels are extremely weather and daylight dependent and can be used only at cloud free conditions during daytime.

There has been a considerable amount of research done about classifying different ice types (Voss, 2003; Walker et al., 2006), but majority of the studies have been focused on

the Artic regions with the aim to differentiate first-year and multi-year ice. In Arctic regions ice has been classified and quantified using passive microwave sensors, e.g. Electrically Scanning Microwave Radiometer (ESMR), Scanning Multichannel Microwave Radiometer (SMMR), and Special Sensor Microwave Imager (SSM/I) (Barry et al., 1993). Unlike optical sensors, passive microwave sensors are not affected by cloud cover or lack of light. However, those sensors offer low spatial resolution, e.g. the SSM/I has a spatial resolution of 12.5 km (NSIDC, 2012). Therefore, passive microwave sensors are not useable to differentiate ice types on small partitioned regions like the Baltic Sea.

Nowadays increasingly Synthetic Aperture Radar (SAR) is being used to measure ice parameters. Today operating SAR carrying satellites part of Copernicus mission are Sentinel-1, Cosmo-SkyMed, Radarsat-2, TerraSAR-X, TanDEM-X and PAZ (ESA, "Synthetic Aperture Radar Missions"). The aim of ice monitoring is to develop an automatic operational system to distinguish between different types of ice. A number of works have focused on using backscattering values to discriminate between ice types and water (Mäkynen and Hallikainen, 2004; Dierking, 2010) which have concluded that using only backscattering values to automatically classify ice types is not sufficient. Other studies that have focused on interferometric properties of the Baltic Sea ice (Dammert *et al.* 1998; Berg *et al*., 2015) prove that coherence data between two consecutive SAR images gives valuable information about ice dynamics. Coherence has been successfully used to distinguish between fast ice and other types (Meyer *et al.*, 2011), but there has been limited research whether it is possible to determine automatically more ice types based on coherence values.

2 OBJECTIVES

This study is focused on studying ice parameters in Western Estonian coastal sea, which includes Gulf of Riga and Väinameri during 2012.

The objective of current study are (i) to determine which polarizations and imaging modes are most suitable for measuring ice parameters using X-band interferometric SAR data. (ii) to develop a method of retrieving ice parameters coherence and backscattering, (iii) to determine the limit values of parameters of observed ice type and (iv) to apply determined limit values of ice type parameters for automatic distinction between ice types in order to create a map of ice types.

3 BACKGROUND

3.1 TanDEM-X

TerraSAR-X (TSX) is operated by German Aerospace Centre (DLR) and was launched in July 2007. Its add-on TanDEM-X (TDX) was launched in June 2010 with purpose to provide global Digital Elevation Model (DEM) of Earth (Gruber et al. 2012). According to Krieger *et al.* (2007) TDX is a rebuilt of TSX with only minor modifications to receive information about status and GPS position broadcasted by TSX. Both satellites are high-performance synthetic aperture radar (SAR) operating in X-band. TerraSAR-Xs, basis for TanDEM-X, nominal orbit height at the equator is 514 km and its revisit cycle is 11 days (Eineder et al. 2008).The central frequency of the instruments is 9.65 GHz (*Ibid.*).

TanDEM-X satellite has two major interferometric operation modes: pursuit monostatic mode and bistatic mode. In the pursuit monostatic mode, the two satellites, TSX and TDX, are operated independently from each other. Satellites are positioned 76 km apart to avoid interference between the radar signals. Bistatic mode uses close together positioned TSX or TDX to transmit signal to Earth's surface. Then the scattered signal is simultaneously recorded by both satellites. TanDEM-X operational modes are illustrated in Figure 1. Interferometric configuration may also be combined different TSX and TDX imaging modes like Stripmap, ScanSAR, Spotlight, and Sliding Spotlight. (Krieger *et al.*, 2007)

The basic SAR imaging mode is Stripmap mode. According to (*Ibid.*), "The ground swath is illuminated with a continuous sequence of pulses while the antenna beam is

pointed to a fixed angle in elevation and azimuth". For Stripmap mode incidence angle range is 20° to 45° and ground range resolution is 1.70 m to 3.49 m.

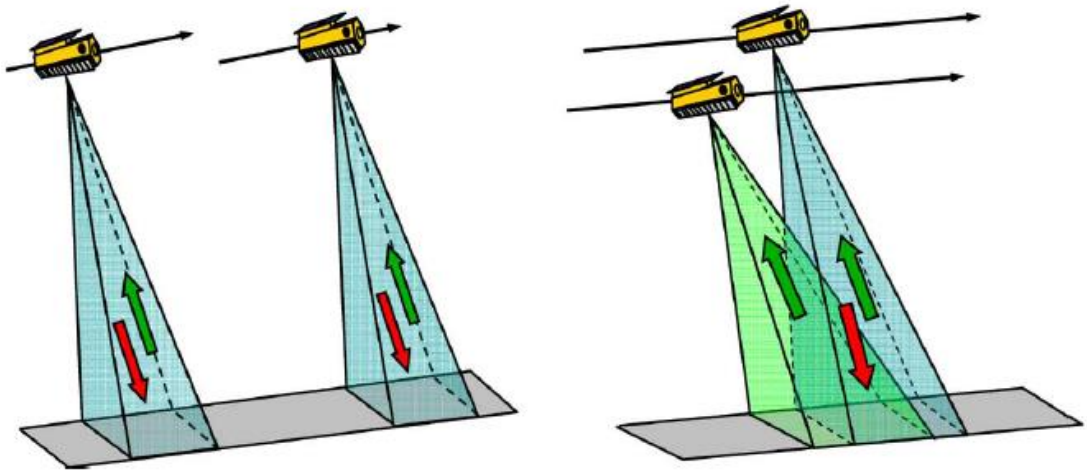

Figure 1: (Krieger *et al.*, 2007) Examples of data acquisition modes for TanDEM-X: pursuit monostatic mode (on the left), and bistatic mode (on the right).

The polarization combinations for TanDEM-X are available in large variety offering single-, dual-, and quad-polarimetric acquisitions (Kugler *et al*., 2014).

3.2 Parameters calculated from interferometric SAR data

Interferometric SAR images allow measuring the topography of a surface, its changes over time and other changes in the detailed characteristics of the surface. This is possible due to phase difference in the signals received by two satellites. The interferometric phase difference can be formed for each imaged point. Surface changes over time can be detected by comparing phases of two images from same site taken at different times. This time difference may vary from fraction of seconds to years. (Rosen *et al*., 2000)

Same method can be used to compare images of different polarizations. Both comparisons are done by calculating correlation coefficient between two images called coherence γ (Moreira *et al.,* 2013).

When electromagnetic wave transmitted from the radar reaches a particular target, it interacts with it. As a consequence, part of the energy carried by the initial wave is absorbed by the target and the rest is reradiated as a new electromagnetic wave. Due to this, properties of the reradiated wave can be used to characterize or identify the target (Lee and Pottier, 2009, p. 53-61). Backscatter is the portion of outgoing radar signal that the target redirects directly back toward the radar antenna (ESA, "RADAR and SAR Glossary").

Properties of the electromagnetic wave are dependent on transmitted and received polarizations. The combined polarization radar image can be HH (horizontal transmitting, horizontal receiving), VV (vertical transmitting, vertical receiving), HV (horizontal transmitting, vertical receiving) or VH (the reverse of HV) ("Polarimetric observation by PALSAR"). After interacting with the surface, the polarisation state may be altered, e.g. the received wave in horizontal polarization may bounce on the surface multiple times and be backscattered as in vertical polarization state (NSIDC, "SAR Theory/Interpreting Images"). Different polarizations therefore detect different surface properties.

Speckle or noise effect can be observed on SAR images that, are caused by the presence of many elemental scatterers with a random distribution within a resolution cell. Due to random distribution of the scatterers, the resulting intensity and phase change from pixel to pixel with exponential and uniform distribution. To reduce the effect of speckle mean and median filters are applied. (Moreira *et al.,* 2013)

Mean filter allows smoothing the image and reduce the amount of intensity variation between side-by-side pixels. The amount of pixels for which the filter calculates the mean value can vary. The usual window sizes are 3x3 and 5x5, but larger window sizes can be used to reduce the weight of one pixel. Median filter ranks the pixel values in the filter window and replaces the centre pixel value according to the ranking. Both median and mean filter reduce the resolution of the image. (Shanthi and Valarmathi, 2011)

4 DATA

4.1 Interferometric TDX SAR data

Coregistered Single look Slant range Complex (CoSSC) product is used in current study. CoSSc product is the basic product of TanDEM-X which contains two SSCs - one of each satellite the passive channel is coregistered to the active channel (Balss *et al.*, 2012).

Three image pairs taken between 3rd and 5th of February 2012 and two images taken between 14th and15th of March 2012 were used in this work. Details about images are presented in Table 1. All images are in Stripmap mode and both, ascending and descending acquisitions were used. Also, images with different incidence angles were used. For all images only co-polarized (HH and VV) data is available.

Table 1: Characteristics of used SAR images.

Image	Date	Centre incidence angle (°)	Polarization mode	Polarizations	Orbit Direction	Operation Mode	Region
A	3.02.2012	46.53	Dual	HH, VV	Ascending	Bistatic	Väinameri
B	4.02.2012	28.22	Single	HH	Ascending	Monostatic	Kihnu
C	5.02.2012	38.78	Dual	HH, VV	Descending	Bistatic	Väinameri
D	14.03.2012	23.37	Dual	HH, VV	Descending	Bistatic	Kihnu
E	15.03.2012	44.94	Dual	HH, VV	Descending	Bistatic	Kihnu

4.2 *In situ* measurements and meteorological data

Fieldwork was conducted between 3rd and 4th of February 2012 and 15th of March 2012 by the Marine System Institute at Tallinn University of Technology. On 3rd and 4th of February 2012 ice was measured on Kuivastu and Virtsu port area, on ferryboat operating between Kuivastu and Virtsu, on Matsalu bay near Saastna peninsula and on Värati bay and on 14th and 15th of March 2012 on bay of Tõstamaa, bay of Värati, near Kastna Nina and Munalaid and on Virtsu port area. During the fieldwork station name, date, time, GPS coordinates, and description of surface were noted. Also photographs of the surface were taken. It has to be noted that for safety reasons and ease of access, all measurements were conducted on ice which was at least 10 cm thick or on ferryboat plying between Virtsu and Kuivastu.

Meteorological data from 1st of January 2012 to 30th of March 2012 is provided by the Estonian Environment Agency. Meteorological data includes daily average temperature and hourly wind speed and direction measurements, temperature and precipitation from the Kihnu coastal station.

4.3 Moderate Resolution Imaging Spectroradiometer data

Data from Moderate Resolution Imaging Spectroradiometer (MODIS) is used for visual estimation of different types of ice. During the period from 29th of January 2012 to 20th of March 2012, 25 images were available that were not greatly affected by cloud cover.

5 METHOD

5.1 SAR backscatter and coherence

Backscattering calculations are based on Airbus Defence and Space (2014). Firstly complex data from area of interest is acquired and digital number (DN) values are calculated using equation (1)

$$DN = \sqrt{I^2 + Q^2} \tag{1}$$

where I is the real part and Q is the imaginary part of the backscattered complex signal.

Radar brightness described by sigma naught β^0 is calculated using digital numbers and applying the calibration factor k_s. Radar brightness represents the radar reflectivity per unit area in slant range.

$$\beta^0 = k_s \cdot |DN|^2 \tag{2}$$

For better understanding, β^0 is converted to dB.

$$\beta_{dB}^0 = 10 \cdot \log_{10}(\beta^0) \tag{3}$$

Backscattering is influenced by local incidence angle. To take this into account, sigma naught is calculated using equations (4) and (5)

$$\sigma^0 = \beta_0 \cdot \sin\theta_{loc} \tag{4}$$

$$\sigma_{dB}^0 = \beta_{dB}^0 + 10\ \log_{10}\sin\theta_{loc} \tag{5}$$

where θ_{loc} is the local incidence angle.

Coherency is calculated using equation (6).

$$\gamma = \frac{\langle s_1 s_2^* \rangle}{\sqrt{\langle s_1 s_1^* \rangle \langle s_2 s_2^* \rangle}} \quad (6)$$

In equation (6) s_1 and s_2 are the complex amplitudes from two different images.

5.2 Relating coherence and backscattering values with ice types and water

To relate coherence and backscattering values with ice types, regions of interest (ROIs) were selected, which represent different ice types and water. ROIs were selected based on optical MODIS images and on data collected during *in situ* measurements. Used ROIs contain at least 500x500 pixels, which gives statistically meaningful representation of observed area. Backscattering values were collected from all the available bands and coherence values were collected from pairs of bands using all variations of available bands. Used steps are described on Figure 2.

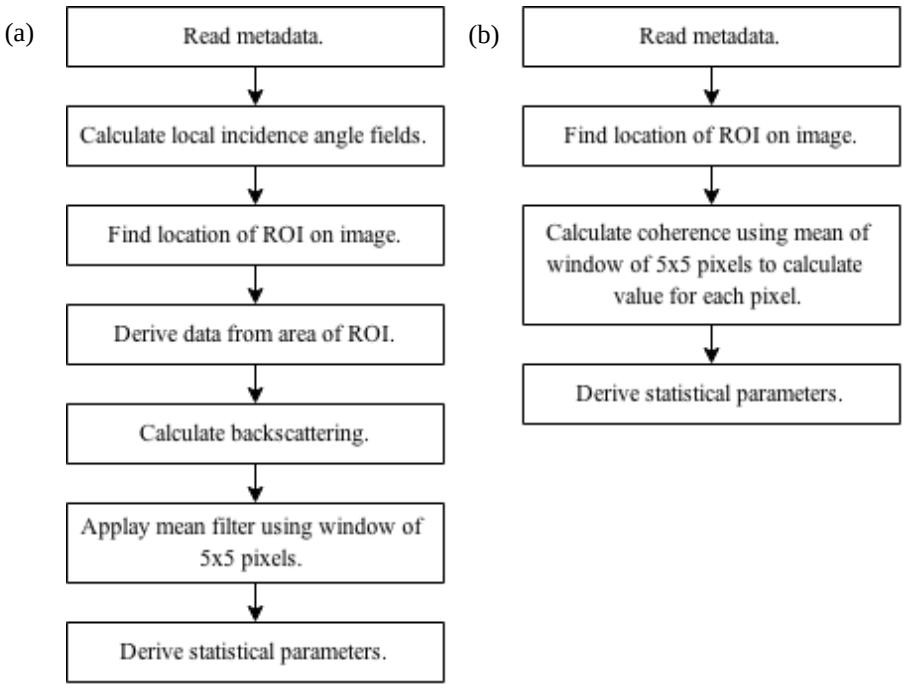

Figure 2 : Flowchart of data processing of SAR images to calculate (a) backscattering and (b) coherence.

6 RESULTS

6.1 Identified ice types

On the studied images water, fast ice, thin smooth ice and pancake ice could be identified. Identification was based on using MODIS images and photographs (examples of ice types is presented in Appendix A), surface descriptions and GPS data from in situ measurements. Fast ice in turn divides to older and younger fast ice, both of which occur on images D and E between Kihnu Island and mainland Estonia. Images C and A also cover Matsalu bay area, where fast ice is present. Matsalu bay is where ice forms earliest in Estonian coastal water and is also living environment for a large amount of coastal plants like *Phragmites*, which could affect the surface roughness of ice. Due to differences in those examples of fast ice, they will be referred accordingly as fast ice (old), fast ice (new) and fast ice (bay).

6.2 Effect of incidence angle and polarization

To analyse the effect of incidence angle and different polarizations on coherence and backscattering, images D and E were used. Images are taken one day apart with similar meteorological conditions. Figure 3 depicts average coherence of water, fast ice (old) and fast ice (new) collected from image D, which has incidence angle of 23.4°. Figure 4 on the other hand depicts the same parameters collected from image E, which has incidence angle of 44.9°. Compeering Figures 3 and 4 it is obvious that images with high incidence

angle show better coherence differentiation between water and different ice types at all polarizations. On images with low incidence angle, measured coherence values are over 0.7 for water and for different ice types. Both fast ice types show extremely similar coherence values, which were around 0.8.

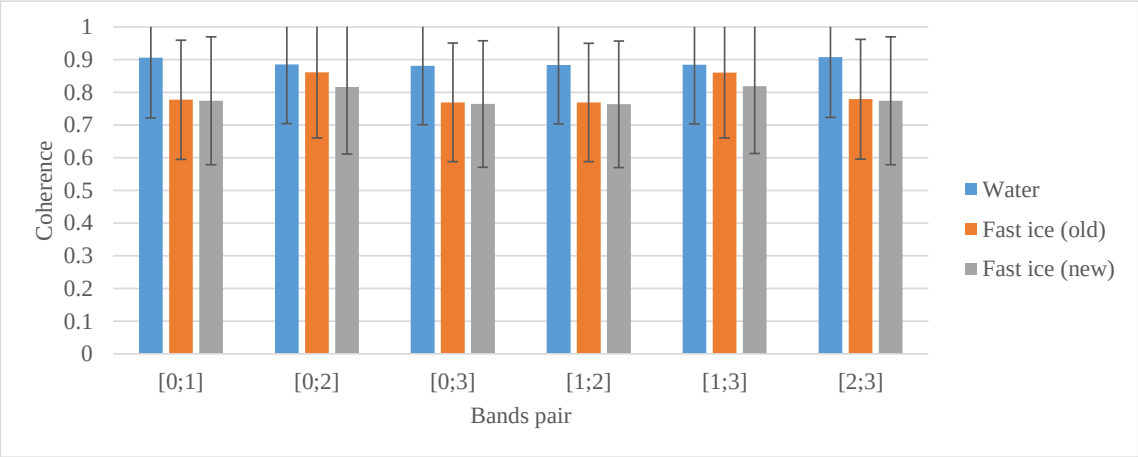

Figure 3: Coherence of water and different ice types of images with low incidence angle (incidence angle equals 23.4°). Numbers on horizontal axis represent different bands (0-HH-Monostatic, 1-HH-Bistatic, 2-VV-Monostatic, 3-VV-Bistatic). Error bars represent average standard deviation of coherence.

Figure 4 also illustrates that the best results are obtained when the coherence pair contains different polarizations but the same acquisition mode. The biggest differences of water and ice type coherences are visible in the pairs HH-Monostatic-VV-Monostatic ([0;2] on Figure 4) and HH-Bistatic-VV-Bistatic ([1;3] on Figure 4), where the difference in mean values is over 0.4. Water and ice is also distinguishable when the coherence pair contains different polarizations and different acquisition modes as in pairs HH-Monostatic-VV-Bistatic ([0;3] on Figure 4) and HH-Bistatic-VV-Monostatic ([1,2] on Figure 4). However in this case different ice types are poorly distinguishable, as both ice types values are positioned closely around 0.6. The worst result for differentiating water and ice types according to coherence is received when the coherence pair contains same polarizations and different acquisition modes as in pairs HH-Monostatic-HH-Bistatic ([0;1] on Figure 4) and VV-Monostatic-VV-Bistatic ([2;3] on Figure 4), where difference

in coherence mean is around 0.1, which is within standard deviation. The difference between different ice types is similar to result received when the coherence pair contains different polarizations and different acquisition mode.

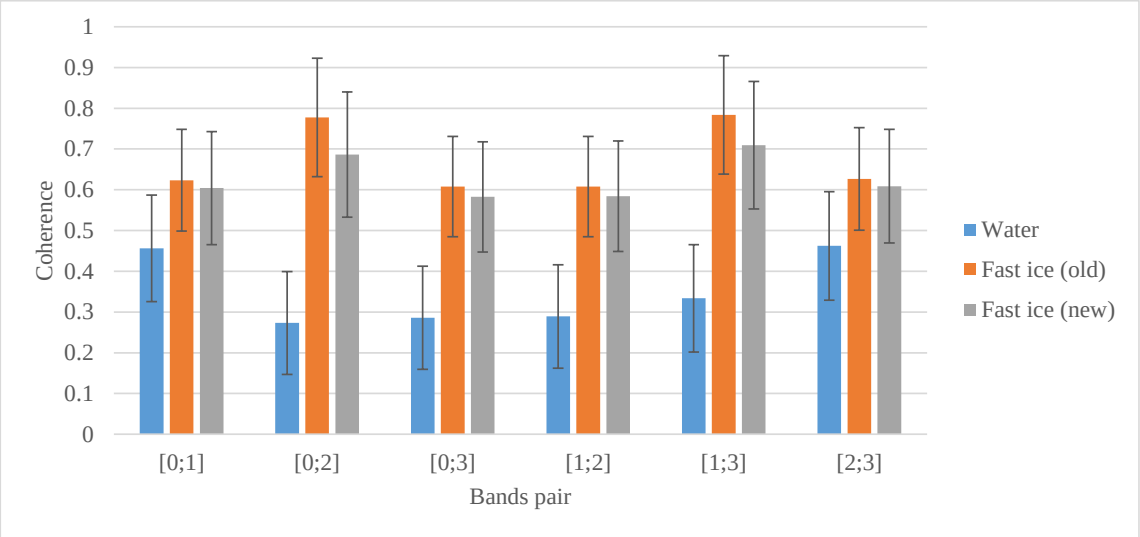

Figure 4: Coherence of water and different ice types of images with high incidence angle (incidence angle equals 44.9°). Numbers on horizontal axis represent different bands (0-HH-Monostatic, 1-HH-Bistatic, 2-VV-Monostatic, 3-VV-Bistatic). Error bars represent average standard deviation of coherence.

Therefore, according to this data, the best way to discriminate between water and ice, is to use coherence pair with different polarizations, HH and VV. To distinguish between different ice types both images in the coherence pair should have the same acquisition mode.

Backscattering of water, fast ice (old) and fast ice (new) is presented on Figure 5. There are no significant changes of backscattering between different polarizations and the difference of backscattering of water and different ice types appears to stay approximately the same for all polarizations. Water can be differentiated from ice using both images with high and low incidence angle. On images with high incidence angle water has lower backscattering values than ice and on images with low incidence angle water has higher backscattering values than ice. However, there are larger differences between ice types when using images with high incidence angle.

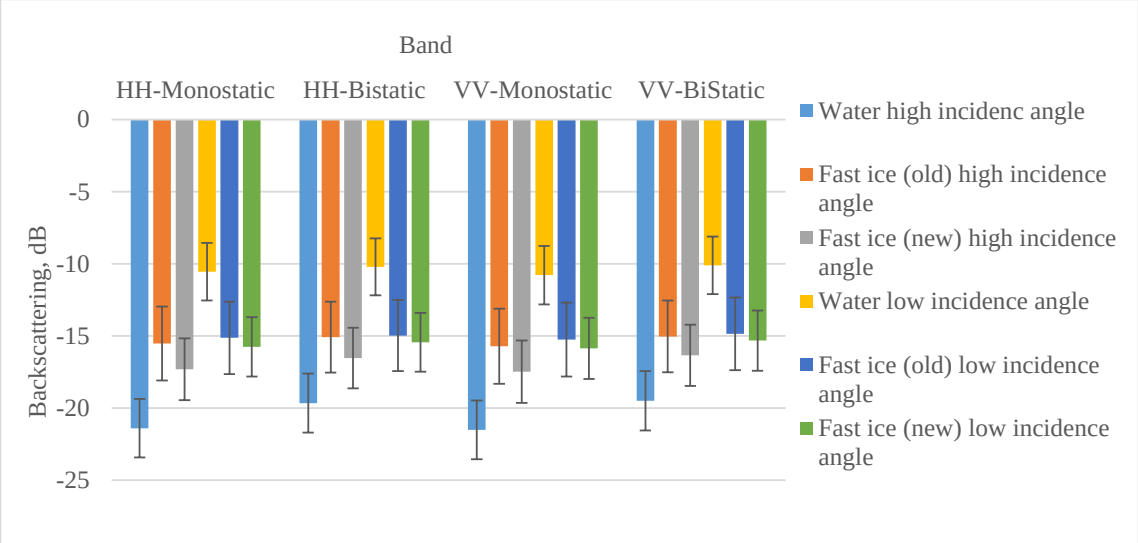

Figure 5: Backscattering of water and different ice types from images with both low and high incidence angle. Error bars represent average standard deviation of backscattering.

6.3 Coherence and backscattering values of different ice types

To attribute certain coherence and backscattering values to different ice types, individual means and standard deviations of backscattering and coherence values of each ROI were calculated. Also means and standard deviations of backscattering and coherence values of all ice types were calculated. From the analysis it can be assumed that besides the mean coherence or backscattering value of certain ice type, standard deviation is also a valuable parameter for describing each ice types.

Figure 6 presents the means and standard deviation of each ROI and each type of ice. Water values were measured at conditions where the wind speed did not exceed 7 m/s. The mean value of coherence of all water ROI values is 0.24 with standard deviation of 0.11, which means that 68% on water values fall between 0.13 and 0.35. The mean backscattering value of water is -21.1 dB, most of the backscattering values fall between -23.4 dB and -18.8 dB.

Fast ice (old), fast ice (new) and fast ice (bay) have large area of coinciding values. Mean coherence of fast ice (old) is 0.80, of fast ice (new) is 0.71 and of fast ice (bay) is 0.82. Accordingly ice types have coherence standard deviation of 0.13, 0.13 and 0.18. Similarly, the backscattering values of fast ice types are situated close together. Fast ice (old) has backscattering of -15.6 dB, fast ice (new) -17.5 dB and fast ice (bay) -21.8 dB with standard deviation values respectively 2.8, 2.3 and 2.5 dB. This means that both backscattering and coherence values of fast ice types overlap greatly.

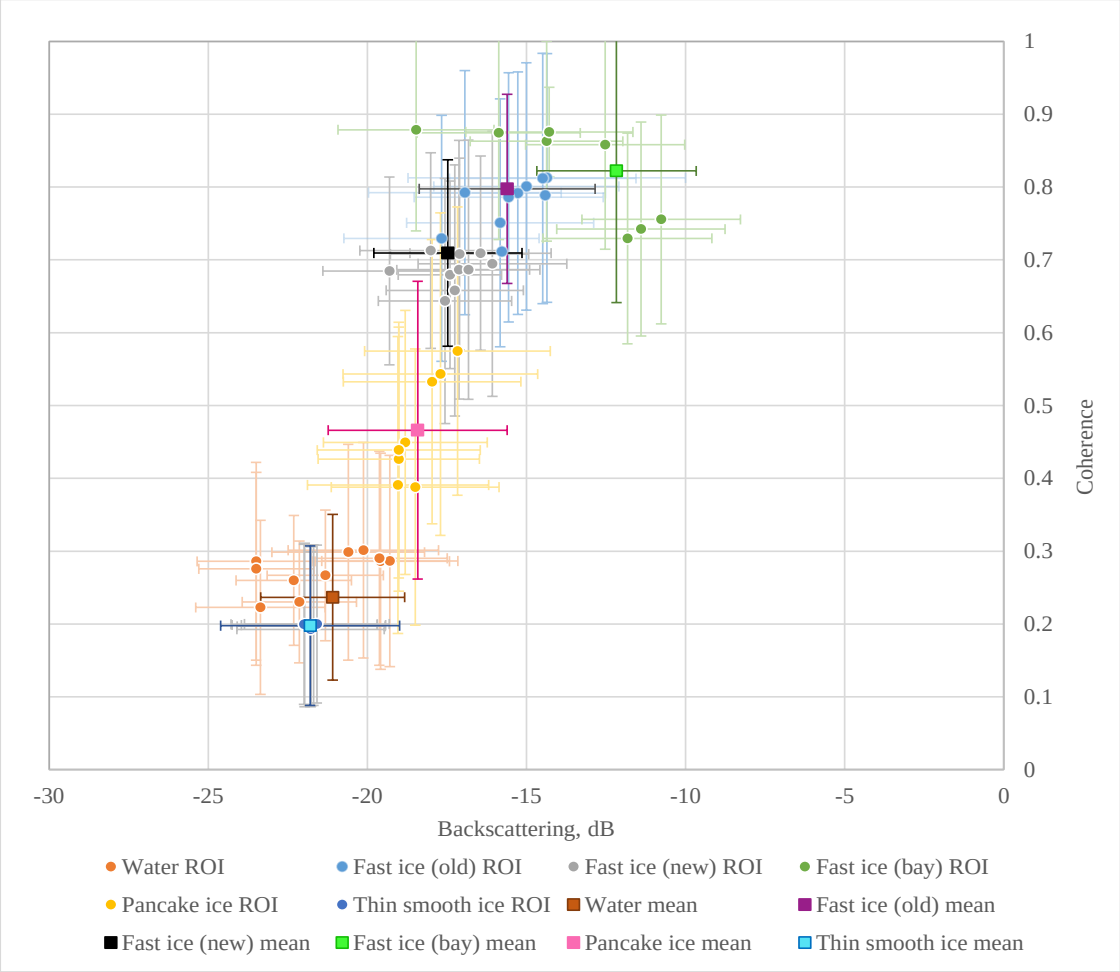

Figure 6: Coherence and backscattering values of water, fast ice, pancake ice and thin smooth ice ROIs using pair HH-Monostatic-VV-Monostatic data for coherence calculation and HH-Monostatic data for backscattering calculations. Error bars represent the standard deviation of each ROI.

It is noteworthy that all thin smooth ice ROI mean values of backscattering and coherence fall closely together. The mean value of coherence for thin smooth ice is 0.20 and mean value of backscattering is -21.8 dB. The corresponding standard deviation values are for thin smooth ice 0.11 and 2.3 dB. Those values are true for all thin ice ROIs with only variance of backscattering by 0.2 dB.

Pancake ice is characterised by its large coherence standard deviation values. The mean coherence value for pancake ice is 0.47 and mean backscattering value is -21.8 dB. The standard deviation for coherence is 0.20 and for backscattering 2.3 dB. All pancake ice ROIs have coherence standard deviation larger than 0.18

6.4 Coherence images for area of interest

Visualising coherence values for the whole area of interest enables to detect ice cracks and other irregularities in ice. Figure 8 represents the appearance of ice cracks in fast ice (old) and fast ice (new) as a line of high coherence values. Due to that, fast ice (old) itself has high coherence values, meaning that ice crack stand out more easily in fast ice (old).

Examining coherence images of the same area but at different times, gives information about formation of ice structures. Figure 7 represents the coherence values during formation of ice structures on the 4th of February 2012 (Figure 7a) and 40 days later (Figure 7b). It has to be noted that same polarizations are not used on coherence calculations on Figure 7a, as only two bands of HH-Monostatic were acquired on the 4th of February 2012. Therefore values of Figure 6 cannot be used to classify ice types on Figure 7a. Nevertheless, there are similar structures visible on both images. The smooth ice surface with low coherence as seen on 4th of February 2012 transformed to ice with high coherence by 15th of March 2012.

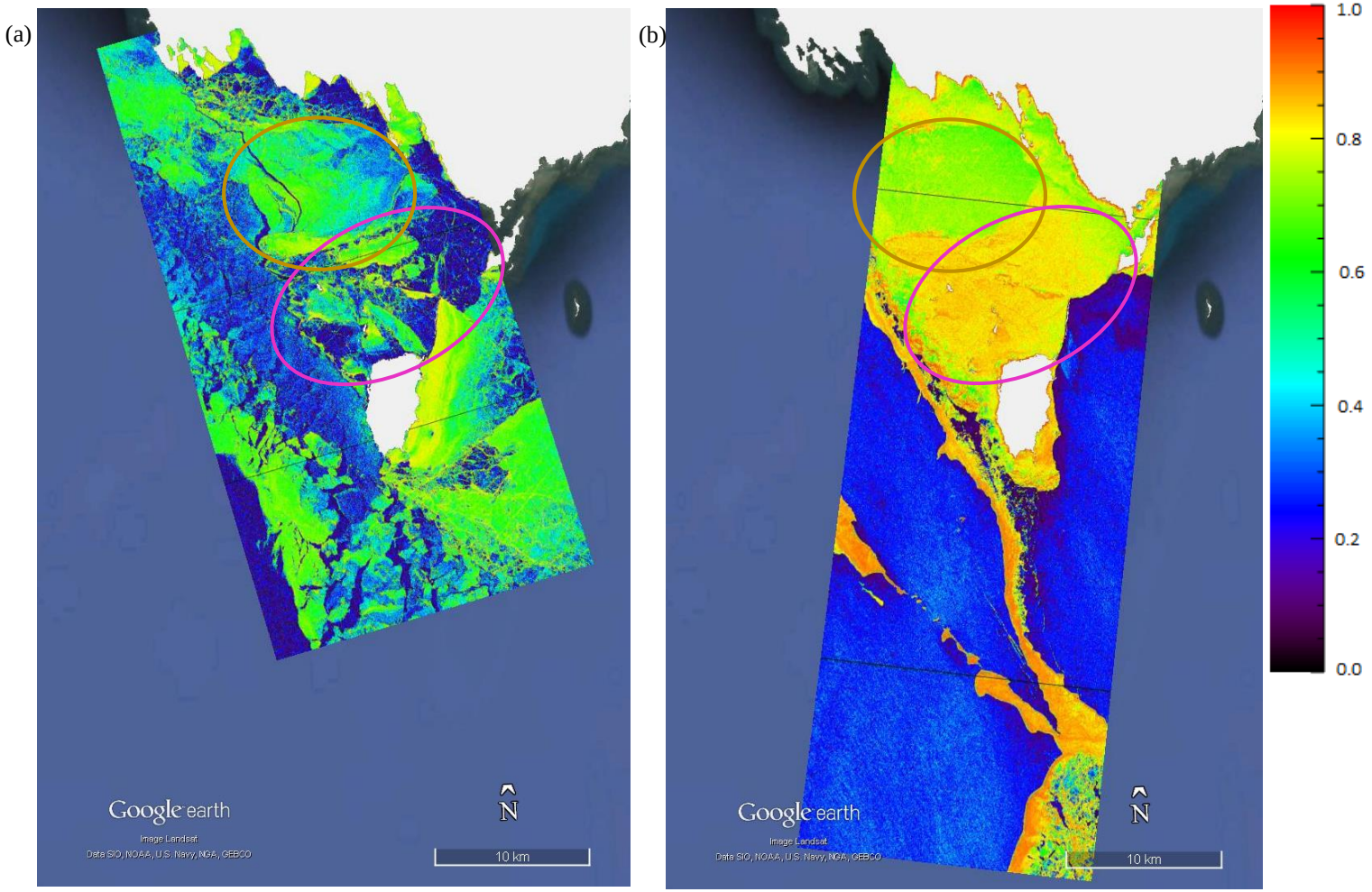

Figure 7: Coherence values around Kihnu Island (a) on 4th of February 2012 using coherence pair HH-Monostatic-HH Monostatic; (b) on 15th of. March 2012 using coherence pair HH-Monostatic-VV-Monostatic. Grey area visualises land. Brown oval refers to area of fast ice (new) and pink oval to area of fast ice (old).

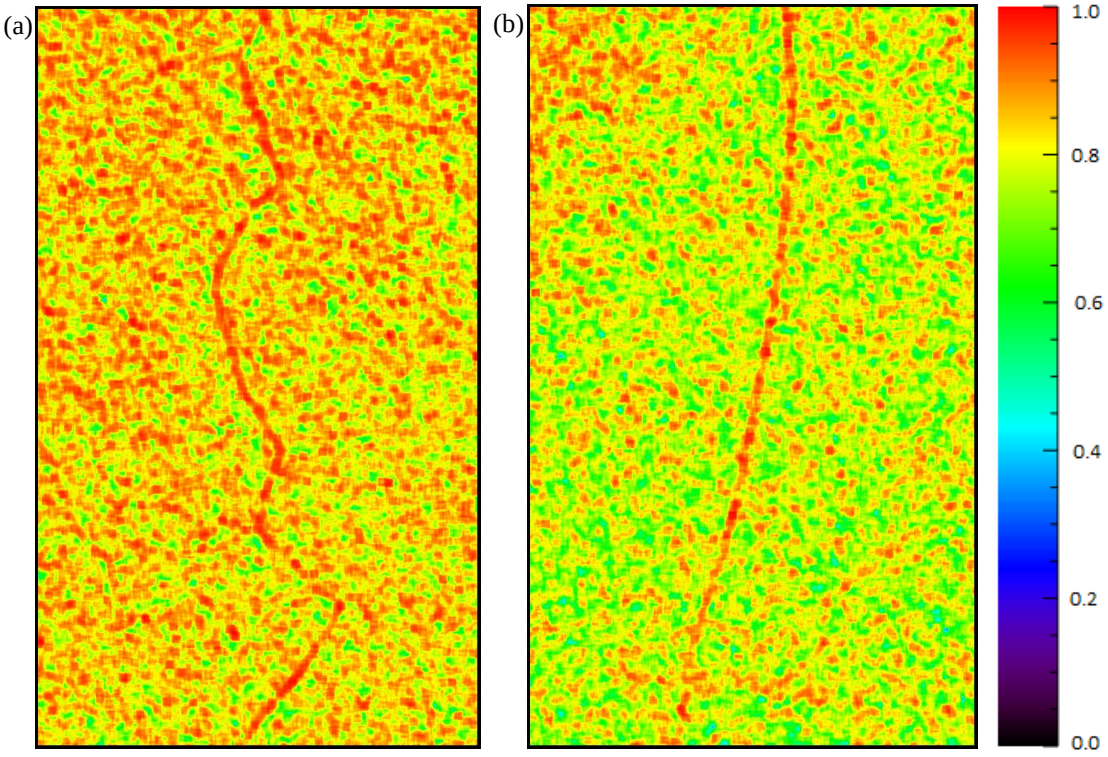

Figure 8: Presence of cracks in ice visible on coherence image. (a) Cracks in fast ice (old). (b) Cracks in fast ice (new).

6.5 Ice map based on coherence and backscattering values

Based on values depicted on Figure 6, ice map of Väinameri on the 3rd of February 2012 is created (Figure 9). Classification is done by classifying 25x25 pixels together, firstly mean coherence and backscattering value for 25x25 pixels is calculated and then based on mentioned values, these 25x25 pixels are classified as fast ice, thin smooth ice or pancake ice. Areas which were falsely classified, were indicated as such by hand and counted as unclassified. Areas of which ice types could be referenced with *in situ* measurements or MODIS images were all correctly classified.

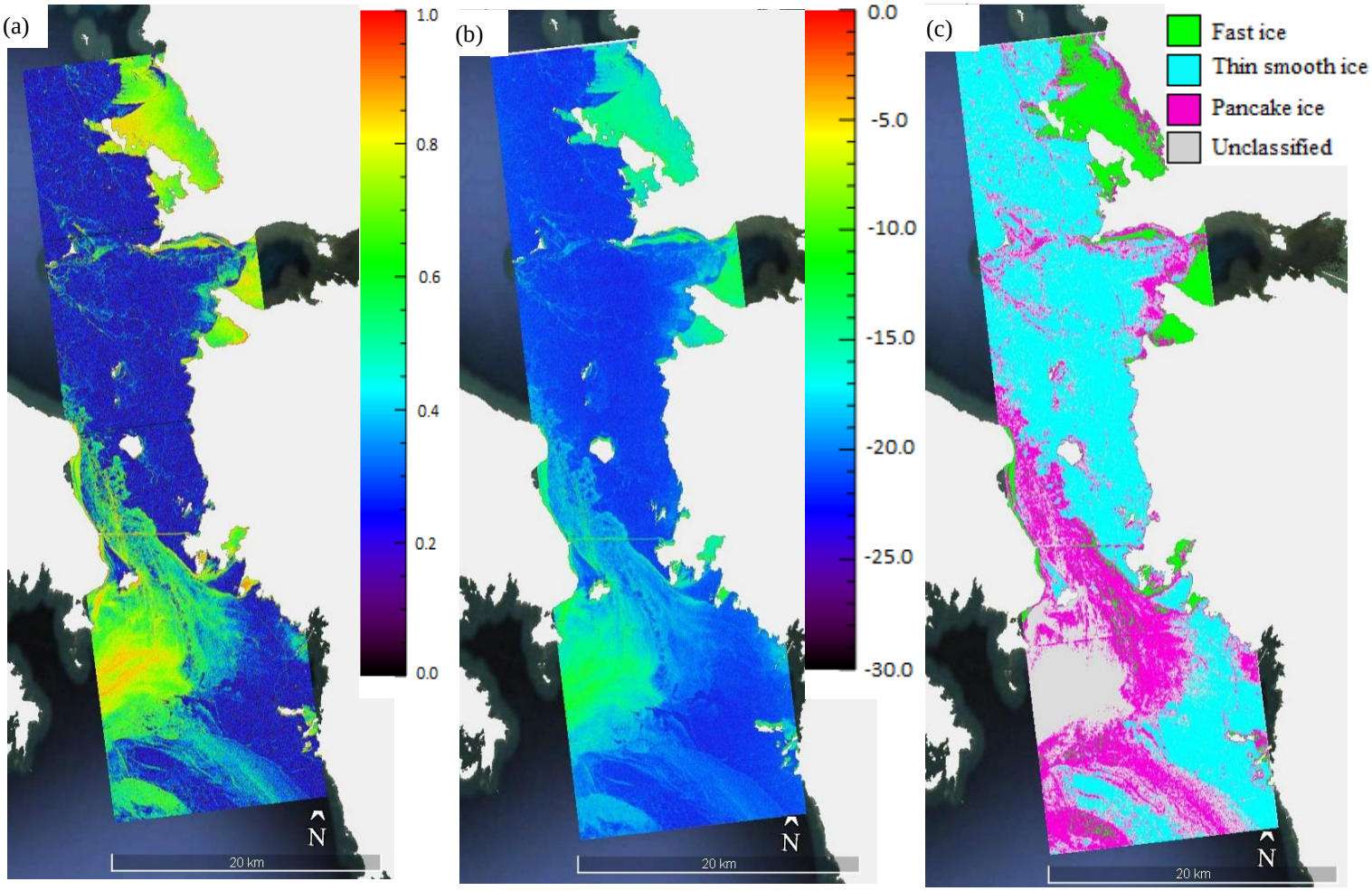

Figure 9: (a) coherence values of image A, (b) backscattering values of image A and (c) map of ice types based on coherence (a) and backscattering (b) values.

7 DISCUSSION

7.1 Limitations to ice type classification

In this work the effect of incidence angle on ice type classification from SAR imagery was studied using comparison of incidence angle of 23.4° and 44.9°. The study concludes that in order to discriminate between different types of ice and water, images with high incidence angle should be used. This is in accordance with Wakabayashi *et al.* (2004), according to whom using L-band SAR data coherence differences of different types of ice are larger at incidence angles exceeding 40°. It was also observed, that in order to distinguish between different types of ice, the imaging mode of images used for coherence calculations, have to be the same. Generally polarimetric SAR is used in monostatic mode (Moreira *et al.*, 2013), but a few studies show that bistatic data could be successfully used as a remote sensing tool (Dubois-Fernandez *et al.*, 2006). On Figure 4 it is visible that bistatic data [1;3] follows similar pattern to monostatic data [0;2].

There could be difficulties in distinguishing between different types of ice and differentiating between water and ice. On Figure 6 it is visible, that water and thin smooth ice could have extremely similar values of coherence and backscattering. In this work there is no example of water and thin smooth ice existing together on the same image. Water and thin smooth ice would have to be discriminated from each other by visual evaluation. When on areas of extremely low coherence values stripes of higher coherence are present, which could represent ice cracks and the area would be classified as thin

smooth ice. If the area is determined to be smooth and without sudden changes of coherence the area could be classified as water.

On Figure 9c there are some areas which were falsely classified. Due to high coherence (Figure 9a) in the area, which could be caused by detached ice pushed together, the area was classified by algorithm as fast ice. However the structure of the ice does not match the characteristics of fast ice.

In order to create ice map using coherence and backscattering values, both coherence and backscattering values have to be averaged. On Figure 6 it is visible that different ice types may have similar individual values, but difference of ice types is visible when average of individual values is calculated. In this work, ice map was created by classifying 25x25 pixel boxes. However, this means that the created ice map has significantly lower resolution that original coherence and backscattering images. On the context of this work, the loss in resolution is insignificant, as coherence and backscattering values are calculated from satellite images of extremely high resolution (0.75 – 1.5 m per pixel).

In order to use this method for operational ice surveying, coherence and backscattering values of more ice types would have to be obtained. There is a possibility of false classification, which on some cases could be detected by visual evaluation.

7.2 Interpretation of multi-source data

On Figure 7b there are two different fast ice types visible, fast ice (new) has coherence values around 0.6 and fast ice (old) has values around and higher than 0.8. On Figure 6 can be seen that fast ice (old) and fast ice (new) can have very similar individual pixel values. The difference is more visible when mean filter is applied as in Figure 7b. Differences in ice types characteristics could be related to different meteorological or situational conditions. On examination of the formation of both ice types using MODIS images (Appendix B), it is visible that ice identified as fast ice (old) was formed between

29th and 30th of January. The ice identified as fast ice (new) can be seen on the MODIS images on the 5th and 6th February. On Figure 10 are depicted daily average, minimum and maximum temperatures during formation of ice and time of SAR image acquisition. Fast ice formed on period, when daily average temperature was around -10° C and fast ice (new) when temperature was around -15° C to -20° C. Therefore, both ice types formed when temperatures were well below zero. The direction of wind was prevailingly from east during formation of fast ice (old) and fast ice (new), with wind speed 2…7 m/s. Wind statistics (Figure 11) suggest that drifting ice from the study area would be rather moving away from study area than accumulate in the area. Therefore, fast ice (old) and fast ice (new) have been formed on site, rather than formed elsewhere and moved to the study site.

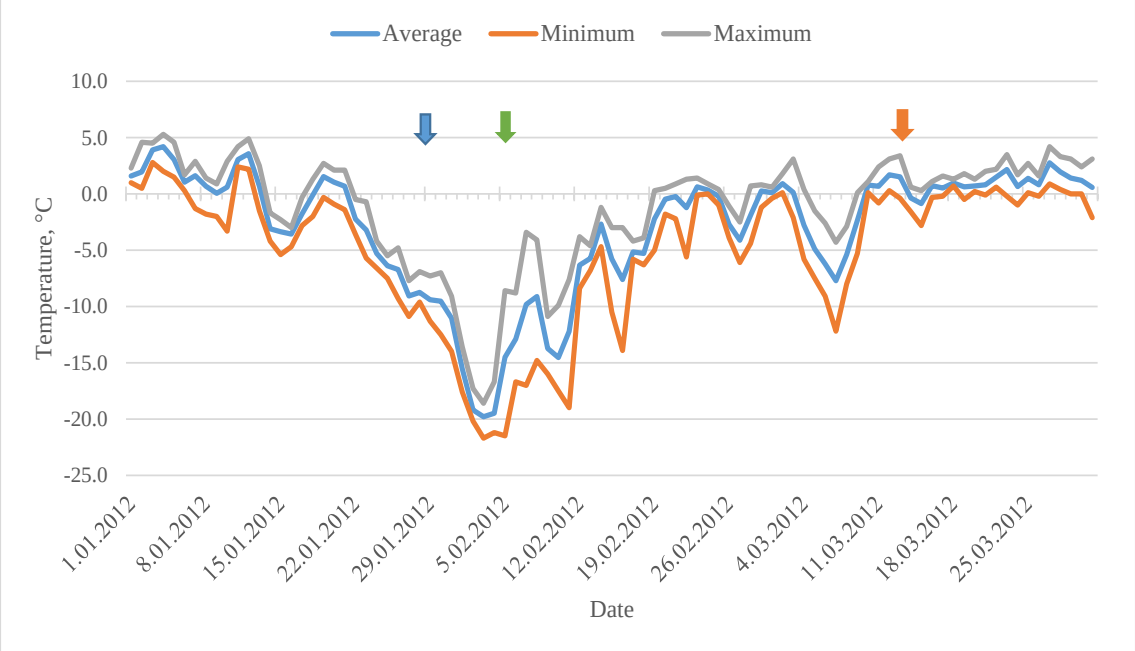

Figure 10: Daily average, daily minimum and maximum temperatures during period between 1st of January 2012 and 31st of March 2012. Blue arrow marks formation of fast ice (old), green arrow formation of fast ice (new) and orange arrow time of SAR acquisition.

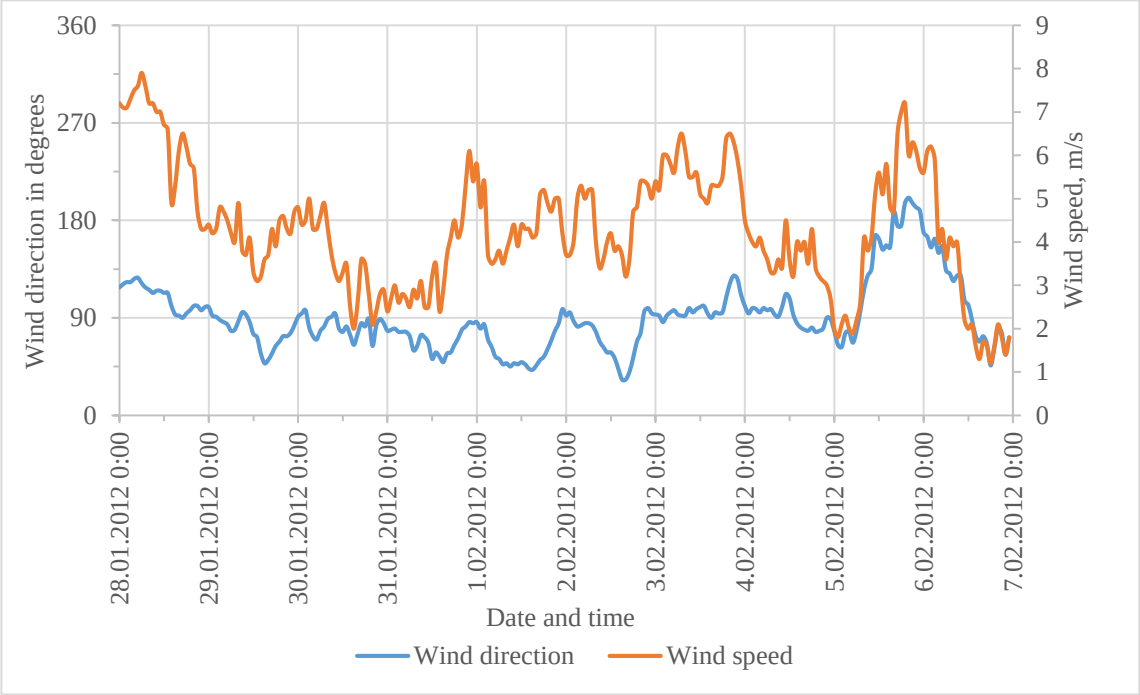

Figure 11: Hourly wind speed and direction during period between 28th of January and 7th of February.

On MODIS images it is visible, that both ice formations stay steady from formation till the time of SAR acquisition. By the time of SAR data acquisition on the 15th of February, fast ice (old) was 45 days old and fast ice (new) was at least 38 days old. This seven day difference between two formations allowed fast ice (old) to grow thicker than fast ice (new).

The later formation of fast ice (new) is likely caused by topographical differences of seafloor. On bathymetric map of the Gulf of Riga (Tsyrulnikov *et al.* 2008) it is visible that area where fast ice (new) was formed, water depth is between 5 to 10 meters, whereas in the area where fast ice (old) was formed, water depth up to 2.5 meters.

CONCLUSION

In this study HH and VV polarizations and Bistatic and Monostatic imaging modes with high and low incidence angel acquisitions were compared to determine the best polarization for backscattering calculations and polarization pair for coherence calculations in order to discriminate between different types of ice. Out of available combinations it appears that the best result is acquired from acquisitions of high incidence angle and coherence pair of HH and VV with the same imaging mode. If wider variance of polarizations and imaging modes are available, new comparison must be done.

Statistical analysis of available ice types was done and threshold values of backscattering and coherence of different ice types were determined. It appears that combination of backscattering and coherence values could be used to automatically distinguish between different ice types. In this study fast ice, thin smooth ice and pancake ice were discriminated from one another. However, some falsely classified areas appeared on ice map, which were determined as false by visual evaluation. In order to use backscattering and coherence values for operational ice surveying continuous data acquisitions must be analysed using SAR images of same incidence angel, polarizations and imaging mode of one area over repeated periods.

In addition to determining ice types, current study shows that interferometric SAR images could be used to examine ice structures. On coherence images of fast ice, cracks in ice can be clearly discriminated from surrounding surface as long thin line of high coherence values. Dots of high coherence values indicate uneven surface. Together with visual satellite images and meteorological data, interferometric SAR data could be used to analyse ice processes and to study how environmental conditions affect ice formation.

ACKNOWLEDGEMENT

Acknowledgements to DLR who provided SAR data, NASA who provided optical MODIS images, and Estonian Environment Agency who provided meteorological data.

The author would like to thank the team of Marine System Institute at Tallinn University of Technology, foremost Rivo Uiboupin, Sander Rikka and Laura Siitam.

LIST OF REFERENCES

Airbus Defence and Space (2014). Radiometric Calibration of TerraSAR-X Data: Beta Naught and Sigma Naught Coefficient Calculation. [WWW] http://www2.geo-airbusds.com/files/pmedia/public/r465_9_tsx-x-itd-tn-0049-radiometric_calculations_i3.00.pdf (30.03.2015)

Balss, U., Breit, H., Duque, S., Fritz, T., Rossi, C. (2012). TanDEM-X Payload Ground Segment, CoSSC Generation and Interferometric Considerations. Document No. TD-PGS-TN-3129. Remote Sensing Technology Institute (Germany).

Banda, O., Goerlandt, F., Montewka, J., Kujala, P. (2015). A risk analysis of winter navigation in Finnish sea areas – *Accident Analysis and Prevention*, 79, 100-116.

Barry, R., Serreze, M., Maslanik, J., Preller, R.H. (1993). The Artic Sea-Ice Climate System – Observation and Modeling. – *Reviews of Geophysics*, 31 (4), 397-422.

Berg, A. Dammert, P. Eriksson, L. (2015). X-Band Interferometric SAR Observations of Baltic Fast Ice – *IEEE Transactions on Geoscience and Remote Sensing*, 53 (3), 1248-1256.

Dammert, P., Leppäranta, M., Askne, J. (1998). SAR interferometry over Baltic Sea ice. – *International Journal of Remote Sensing*, 19 (16), 3016-3037.

Dierking, W. (2010). Mapping of Different Sea Ice Regimes Using Images From Sentinel-1 and ALOS Synthetic Aperture Radar – *IEEE Transactions on Geoscience and Remote Sensing*, 48 (3), 1045-1058.

Dubois-Fernandez, P., Cantalloube, H., Vaixan, B., Krieger, G., Horn, R., Wendler, M., Giroux, V. (2006) ONERA-DLR bistatic SAR campaign: planning, data acquisition,

and first analysis of bistatic scattering behaviour of natural and urban targets. – *IEE Proceedings Radar, Sonar and Navigation*, 153 (3), 214-223.

Gruber, A., Wessel, B., Huber, M., Roth, A. (2012). Operational TanDEM-X DEM calibration and first results - *ISPRS Journal of Photogrammetry and Remote Sensing*, 73, 39-49.

Eineder, M., Fritz, T., Mittermayer, J., Roth, A., Boerner, E. and Breit, H. (2008). TerraSAR-X Ground Segment, Basic Product Specification Document. No. TX-GS-DD-3302. CLUSTER APPLIED REMOTE SENSING (CAF) OBERPFAFFENHOFEN (GERMANY).

ESA. [date unknown]. RADAR and SAR Glossary. [WWW] https://earth.esa.int/handbooks/asar/CNTR5-2.htm (12.03.2015).

ESA. [date unknown]. Synthetic Aperture Radar Missions. [WWW] http://www.esa.int/Our_Activities/Observing_the_Earth/Copernicus/SAR_missions (07.03.2015).

Krieger, G., Moreira, A., Fielder, H., Hajnsek, I., Werner, M., Younis, M., Zink, M. (2007). TanDem-X: A Satellite Formation for High-Resolution SAR Interferometry - *IEEE Transaction on Geoscience and Remote Sensing*, 45, 3317-3341.

Kugler, F., Schulze, D., Hajnsek, I., Pretzsch, H., Papathanassiou, K. (2014). TanDEM-X Pol-InSAR Performance for Forest Height Estimation. – *IEEE Transactions on Geoscience and Remote Sensing*, 52 (10), 6404-6422.

Lee, J., Pottier, E. (2009). Polarimetric radar imaging: from basics to applications. Boca Raton, Florida: CRC Press.

Polarimetric observation by PALSAR [date unknown]. [WWW] http://www.eorc.jaxa.jp/ALOS/en/img_up/pal_polarization.htm (15.05.2015).

Rosen, P., Hensley, S., Joughin, I., Li, F., Madsen, S., Rodriguez, E., Goldstein, R. (2000). Synthetic Aperture Radar Interferometry. – *Proceedings of the IEEE*, 88 (3), 333-382.

Meyer, F., Mahoney, A., Eicken, H., Denny, C., Druckenmiller, H., Hendricks, S. (2011). Mapping arctic landfast ice extent using L-band synthetic aperture radar interferometry. – *Remote Sensing of Environment*, 115, 3029-3043.

Moreira, A., Prats-Iraola, P., Younis, M., Krieger, G., Hajnsek, I., Papathanassiou, K. (2013). A Tutorial on Synthetic Aperture Radar. – *IEEE Geoscience and Remote Sensing Magazine*, 1 (1), 6-43.

Mäkynen, M., Hallikainen, M. (2004). Investigation of C- and X-band backscattering signatures of Baltic Sea ice. – *International Journal of Remote Sensing*, 25 (11), 2061-2086.

NSIDC. (2012). Enhanced-Resolution SSM/I and AMSR-E Daily Polar Brightness Temperatures. [WWW] http://nsidc.org/data/docs/daac/nsidc0464_enhanced_ssmi_amsre_tbs/index.html (07.04.2015).

NSIDC. (date unknown) SAR Theory/Interpreting Images. [WWW] https://nsidc.org/data/radarsat/pdfs/SARTheory.pdf (15.05.2015)

Shanthi, I., Valarmathi, M. (2011). Speckle Noise Suppression of SAR Color Image using Hybrid Mean Median Filter. – *International Journal of Computer Applications*, 31 (9), 14-2.

Statistika andmebaas. [online database] http://pub.stat.ee/px-web.2001/dialog/statfile2.asp (13.05.2015)

Tsyrulnikov, A., Tuuling, I., Hang, T. (2008). Stream lined topographical features in and around the Gulf of Riga as evidence of Late Weichselian glacial dynamics. – *Geological Quarterly*, 52 (1), 81-89.

Vihma, T., Haapala, J. (2009). Geophysics of sea ice in the Baltic Sea: A review. – *Progress in Oceanography*, 80, 129-148.

Voss, S., Heygster, G., Ezraty, R. (2003). Improving sea ice type discrimination by the simultaneous use of SSM/I and scatterometer data. – *Polar Research, 22*(1), 35-42.

Wakabayashi, H., Matsuoka, T., Nakamura, K., Nishio, F. (2004). Polarimetric Characteristics of Sea Ice in the Sea of Okhotsk Observed by Airborne L-Band SAR. – *IEEE Transaction on Geoscience and Remote Sensing*, 42 (11), 2412-2425.

Walker, N., Partington, K., Van Woert, M., Street, T. (2006). Arctic Sea Ice Type and Concentration Mapping Using Passive and Active Microwave Sensors. – *IEEE Transaction on Geoscience and Remote Sensing*, 44 (12), 3574-3584.

APPENDICES

Appendix A. Examples of fast ice (old), thin smooth ice and pancake ice

Figure 1: Photo of fast ice (old) surface.

Figure 2: Photo of thin smooth ice surface.

Figure 3: Photo of pancake ice surface.

Appendix B. MODIS images of Gulf of Riga from 29. January to 6. February 2012

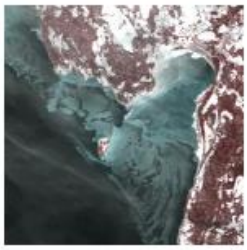

29. January

30. January

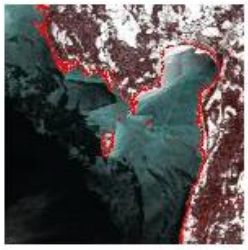

31. January

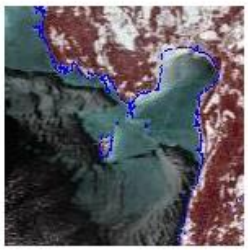

1. February

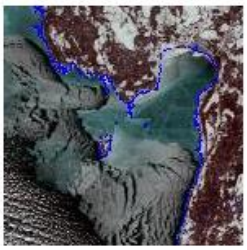

2. February

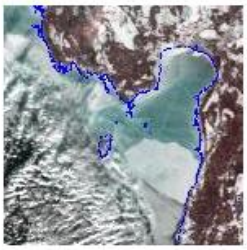

5. February

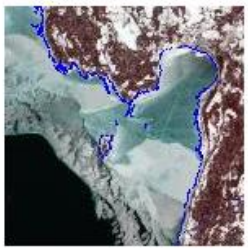

6. February